ACS Photonics

Article

pubs.acs.org/journal/apchd5

Reconfigurable Semiconductor Phased-Array Metasurfaces

Prasad P. Iyer, Nikita A. Butakov, and Jon A. Schuller*

Electrical and Computer Engineering Department, University of California Santa Barbara, Santa Barbara, California 93106, United States

Supporting Information

ABSTRACT: Phased-array metamaterial systems are enabling new classes of refractive and diffractive optical elements through spatial-phase engineering. In this article, we develop design principles for reconfigurable optical antennas and metasurfaces. We theoretically demonstrate the tunability of infrared scattering phase and radiation patterns in low-loss, high-index dielectric resonators using free carrier refraction. We demonstrate reconfigurable endfire antennas based on interference between multiple elements. Within single resonators, we demonstrate reconfigurable broadside antenna radiation lobes arising from interfering electric and magnetic dipole resonances. Extending this concept to infinite arrays, we design ideal Huygens metasurfaces with spectrally overlapping electric and magnetic dipole resonances. By introducing free charge carriers into these metasurfaces, we demonstrate continuously tunable transmission phase between 0 and 2π with less than 3 dB loss in intensity. Such tunable metasurfaces may form the basis for reconfigurable metadevices that enable unprecedented control over the electromagnetic wavefront.

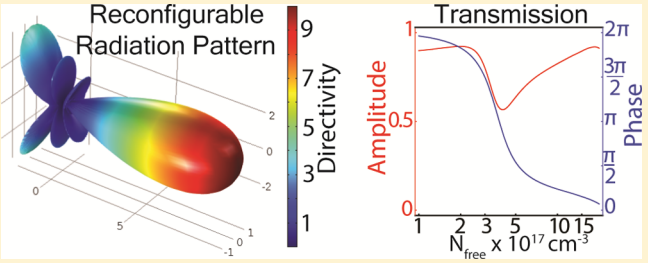

KEYWORDS: *Mie resonators, optical antennas, metasurfaces, III−V plasmonics, phased-array optics*

Antenna and metamaterial systems that can dynamically steer optical-frequency beams constitute a pivotal area of research with applications ranging from Lidar technologies[1] and sensors[2,3] to inter- and intrachip communication[4] in nanophotonic circuits. Steering of beams with metamaterials requires the ability to continuously tune the phase of scattered, reflected, or transmitted waves between 0 and 2π. Thus, there has been extensive research to construct devices that control the phase of scattered waves in a low-loss manner.[5] Metamaterial devices that exploit phase engineering include flat optical elements,[6] polarization converters,[7−9] holographic projectors,[10] and optical vortex beam generators.[11] Arbitrary control of the wavelength-dependent phase enables the miniaturization of bulk refractive (linear) and diffractive (interference-based) optical elements to metamaterial-based devices.[12−14]

Phased-array metamaterials and metasurfaces comprise assemblies of engineered optical antennas. Optical antenna systems that control the phase of transmitted, reflected, or scattered fields have mainly been built from metallic elements. Researchers have demonstrated numerous metallic optical antennas based on scaled-down bow-tie,[15] patch,[16] and split-ring[17] radiofrequency design principles for extreme concentration of light.[18] These single-element antennas typically emit dipolar radiation patterns. By exploiting phased-array concepts, multielement optical antenna systems can support directional radiation patterns. Examples include Yagi−Uda antennas[19,20] and transmitting[12] or reflecting[21−24] infrared metasurfaces, wherein the optical phase is engineered through the antenna shape and size.[25] A broader challenge is to achieve such metamaterial phased arrays in a reconfigurable manner. To achieve reconfigurable properties, researchers have considered electromechanically tuning of the resonator dimensions,[26] phase-change-media-based antennas,[27] graphene-based modulators,[28,29] and charge-carrier-modulation-based designs to tune the background index of the resonators.[30,31] In contrast, we describe an approach for designing reconfigurable, low-loss phased-array metasurfaces by modulating the refractive index of the resonator elements directly. Specifically, we demonstrate infrared antenna and metasurface systems comprising semiconductor optical resonator elements whose response can be tuned via free-carrier refraction.

Semiconductor and dielectric optical antennas have recently emerged as alternatives to plasmonic materials in metamaterial,[6] light-trapping,[32,33] nanoscale optoelectronic,[34] and thermal[35,36] applications. High refractive index (e.g., silicon and III−V compound semiconductors) subwavelength structures exhibit overlapping multipolar resonances, enabling control over antenna emission patterns[37−39] beyond that of dipole antennas. Furthermore, at sub-band-gap frequencies, negligible dissipation ensures that the multipolar scattering cross sections reach fundamental size- and material-independent limits.[40] Researchers have recently demonstrated nontunable dielectric metasurfaces that exploit overlapping multipolar resonances[41,42] or use of the geometric Berry−Pancharatnam phase.[43] Here we exploit an additional advantage of semiconductor materials, namely, the ability to tune the optical constants through

Received: March 18, 2015
Published: June 17, 2015

DOI: 10.1021/acsphotonics.5b00132
ACS Photonics 2015, 2, 1077−1084

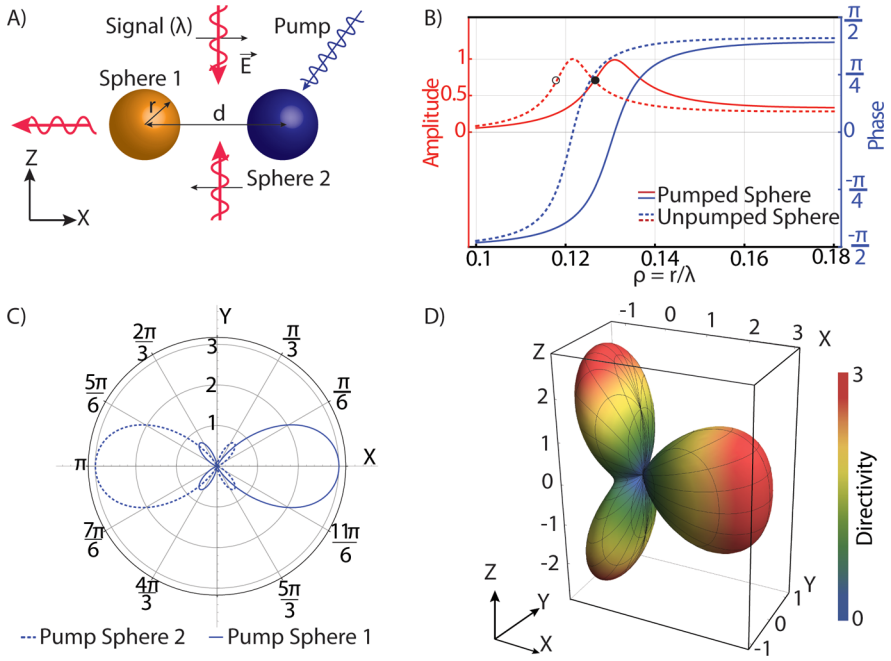

Figure 1. (A) Schematic of a reconfigurable endfire antenna operating at λ = 10.6 μm. The antenna comprises spheres of radius r = 1.34 μm separated by a distance $d = 3\lambda/4$ = 7.95 μm that are illuminated by a standing wave (represented by two counterpropagating linearly polarized plane waves) and placed at electric field nodes in order to excite only MD resonances. (B) Plot of the amplitude (red, left axis) and phase (blue, right axis) of the pumped (solid lines) and unpumped (dashed lines) MD Mie coefficient (b_1) as a function of the normalized size parameter for an InSb sphere. Two unpumped spheres of different sizes (solid and open circles) have different scattering phases with equal amplitudes and can produce a unidirectional lobe (Figure S2 in the Supporting Information). Alternatively, the phase shift can be achieved for a single size (solid circle) by introducing free carriers. At a carrier concentration of 3.1×10^{17} cm^{-3}, the phase shift from the unpumped state is $\pi/2$. (C) Polar plot showing the directivity of the endfire antenna structure in the X–Y plane under two different pumping conditions. The lobe switches directions depending on which particle has been pumped with charge carriers. (D) The three-dimensional radiation pattern of the designed endfire antenna is focused along the $\hat{x}$ axis.

electro-optic effects. Specifically, we theoretically investigate tuning of the scattering phase in infrared semiconductor antennas via free-carrier refraction. We demonstrate multiparticle antenna arrays that function as reconfigurable endfire and broadside antennas. Extending this concept to an infinite array of indium antimonide (InSb) resonators, we develop a design principle for a reconfigurable Huygens metasurface to control the phase and amplitude of the transmitted wave.

The scattering response of spherical dielectric resonators can be calculated analytically with Mie theory[44,45] by decomposing the scattered fields as a sum of individual multipolar resonances. The scattered fields arise from a series of electric and magnetic multipole resonances with Mie coefficients a_j and b_j, respectively, where j refers to the multipole order (i.e., dipole (j = 1), quadrupole (j = 2), etc.). The phases and amplitudes of the scattered fields depend on the magnitudes and phases of the complex Mie coefficients $a_j = |a_j| \exp(i\phi_{a_j})$. In Figure 2B we calculate the phase and amplitude of dipole resonances for an InSb sphere as a function of the normalized size parameter $\rho = r/\lambda$, where r is the radius and λ is the wavelength, assuming sub-band-gap excitation where losses are negligible. The response of sufficiently subwavelength particles (ρ < 0.18) is dominated by magnetic dipole (MD) (ρ = 0.122) and electric dipole (ED) (ρ = 0.164) modes; all of the higher-order modes contribute negligibly to the scattering properties considered in this work. Near the resonances, the scattering phase changes rapidly as a function of the normalized size parameter and the refractive index. This behavior can be leveraged to control the relative phase and thus the directivity of multiparticle antennas.

RESULTS

Endfire Antenna. Consider the simple case of a two-element unidirectional endfire antenna illuminated by an $\hat{x}$-polarized incident plane wave traveling along the $+\hat{z}$ direction (Figure 1A). First, we examine the interference of the scattering from just the MD modes. We can selectively excite the MD modes in the spheres under plane-wave excitation by placing them at a half-wavelength distance above a metal substrate. The reflection of the plane wave forms a standing-wave pattern, causing the electric field to interfere destructively at the center of the sphere. By positioning the spheres at the nodes of the electric or magnetic fields, the MD and ED modes can be individually isolated (Figure S1 in the Supporting Information). Here, for ease of simulation, we isolate the mode using standing-wave illumination. In an endfire configuration, the antennas scatter the normal incident plane wave to a unidirectional lobe oriented along the x axis. The phase response of the scattered field has two components, a particle spacing (d)-dependent traveling-wave phase accumulation (ϕ_d) and a relative phase shift (ϕ_p) that depends on differences in antenna size or refractive index. For constructive interference along the $+\hat{x}$ direction, we must have $\phi_d + \phi_p = 0$; for simultaneous complete destructive interference along $-\hat{x}$, we must have $\phi_d - \phi_p = \pi$ in addition to equal scattering amplitudes. The solution to the simultaneous phase requirements is $\phi_d = -\phi_p = \pi/2$, which leads us to set the distance between the spheres, d, as an odd-integer multiple of $\lambda/4$. We choose the smallest value, $d = 3\lambda/4$, to ensure that the spheres do not overlap ($d > 2r$) and grating side lobes are minimized

DOI: 10.1021/acsphotonics.5b00132
ACS Photonics 2015, 2, 1077–1084

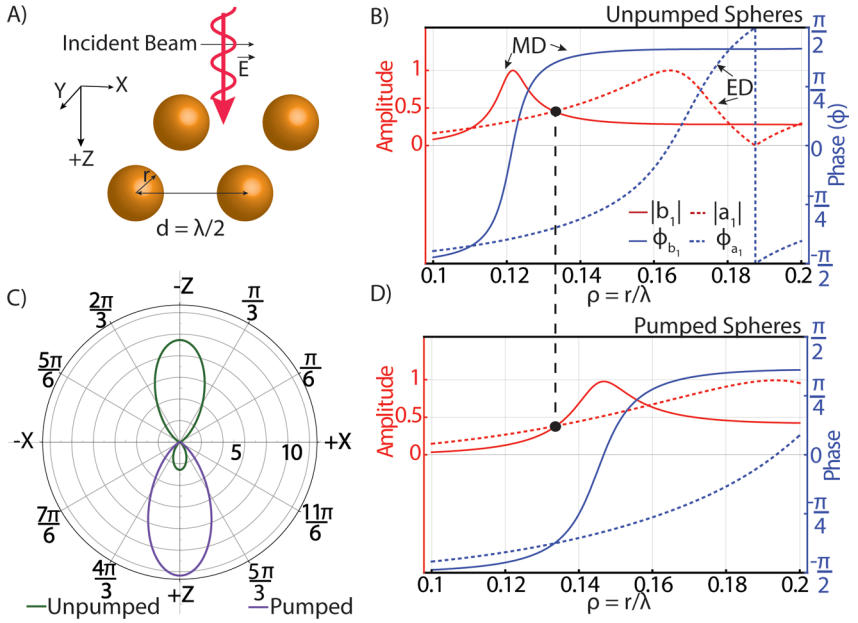

Figure 2. (A) Schematic of a broadside antenna operating at λ = 10.6 μm. Spheres of uniform radius (1.41 μm) are arranged into a square configuration with a spacing of $d = \lambda/2$ = 5.3 μm. The array is illuminated by a normal-incidence plane wave. (B) Plot of the amplitude (red, left axis) and phase (blue, right axis) of the MD Mie coefficient b_1 (solid lines) and the ED Mie coefficient a_1 (dashed lines) as functions of the normalized size parameter in the unpumped state. The black solid circle shows the operating point where b_1 and a_1 are maximally out of phase (green curve in panel c). (C) Directivity of the broadside antenna in the $X-Z$ plane showing the unidirectional lobe in the unpumped (green) and pumped (purple) states. In both cases the ED and MD amplitudes are equal, and the radiation pattern is rotationally symmetric about the Z axis. (D) Shift in the Mie coefficients due to pumping of charge carriers into the resonators at a density of 7×10^{17} cm^{-3}. At the operating condition (black solid dot), the Mie coefficients are exactly in phase when charge carriers are introduced into the resonators (purple curve in panel c).

(see section S2 in the Supporting Information). Unpumped particles of size ρ = 0.118 (open circle in Figure 1B) and ρ = 0.126 (solid circle in Figure 1B) are detuned to the left and right of resonance, respectively. As such, they have identical scattering amplitudes with a $\pi/2$ difference in scattering phase, fulfilling the design requirements. The radiation pattern of such a two-element antenna exhibits a highly unidirectional main lobe (Figure S3 in the Supporting Information).

Such geometric-based phase engineering is at the heart of nearly all directional optical antennas and metasurfaces. Achieving reconfigurable (or tunable) phasing would enable new paradigms in metadevices. For any dielectric or semiconductor, the MD and ED resonances occur at defined eigenvalues $n\rho$ (0.48 for MD and 0.63 for ED). Thus, by changing the particle's refractive index (n) rather than its size (ρ), one can tune the resonance frequencies and shift the associated scattering phase. For operation near the MD resonance, a change in the real part of refractive index of Δn_{MD} = 5% is required. Shifts of this magnitude can be achieved by free-carrier refraction, i.e., introducing free charge carriers into the semiconductor.[46,47] The charge carrier density can be modulated electrically or optically, as considered here, by pumping with a visible-frequency light source.[48,49] Optical pump−terahertz probe studies in a variety of materials revealed free-carrier-induced changes in the complex refractive index described by simple Drude models.[50] III−V compound semiconductors with their low effective masses and high refractive indices are highly suitable materials for free-carrier-refraction-based mid-infrared photonic systems.[51,52] The Drude parameters of InSb used in these calculations (see section S4 in the Supporting Information) are based on conservative estimates of the scattering rate (Γ = 1 THz) and effective mass (m^*_{opt} = 0.014) deduced from experimental data.[53,54] At infrared frequencies, the introduction of free carriers (N_{free}) leads to a decrease (increase) in the real (imaginary) part of the refractive index. For small changes, these shifts are given by

$$\Delta n \approx \frac{-e^2}{2\sqrt{\epsilon_\infty}\epsilon_0 m_{opt}} \frac{\Delta N_{free}}{\omega^2 + \Gamma^2} \quad (1)$$

and

$$\Delta k \approx \frac{e^2}{2\sqrt{\epsilon_\infty}\epsilon_0 m_{opt}} \frac{\Gamma \Delta N_{free}}{\omega^2 + \Gamma^2} \quad (2)$$

respectively. Here, we consider an operating wavelength of 10.6 μm, which falls within an atmospheric transmission window and corresponds to emission of CO_2 gas lasers.

In Figure 1B, we plot the amplitude and phase of the Mie coefficient b_1 in an InSb sphere assuming a carrier density of 3.1 $\times 10^{17}$ cm^{-3} (videos of the evolution of the Mie coefficient with free carriers are available in the Supporting Information). The decrease in Re[n] shifts the resonance toward higher ρ. Although there is an accompanying increase in damping (increase in Im[n]), the effect is weak, and the resonance line shape and amplitude are nearly unchanged. The minimal effect of losses arises from the fact that these dielectric resonators are primarily radiation-broadened.[40] As a result, one can construct a reconfigurable endfire antenna employing the same basic design principle as the geometric approach described above. Two identically sized particles (ρ = 0.126) are initially detuned to the right of resonance (solid circle in Figure 1B). Upon the introduction of free carriers into one of the spheres, it becomes detuned to the left of resonance, inducing a phase shift of $\pi/2$ with negligible change in amplitude. The associated directional radiation pattern is plotted in Figure 1D. There are two side

DOI: 10.1021/acsphotonics.5b00132
ACS Photonics 2015, 2, 1077−1084

lobes pointing approximately along the $+\hat{z}$ and $-\hat{z}$ axes (see section S2 in the Supporting Information). The primary radiation lobe is reconfigurable, pointing to the right or left depending on which of the two particles is optically pumped.

Broadside Antenna. In the previous section, we considered the interference of multiple antennas operating about a single MD resonance. In general, however, dielectric Mie resonators exhibit overlapping multipolar resonances. The interference of MD and ED modes within a single particle can also lead to directional radiation patterns.[37] In the Kerker condition,[55] for instance, the ED and MD modes of a single sphere exhibit equal amplitudes and phases, ensuring complete forward scattering (Figure 2C). Similarly, when the ED and MD modes have equal amplitudes but are π out of phase, the sphere exhibits complete backward scattering. Thus, by tuning the relative phase of the ED and MD resonances we can potentially design a broadside antenna that dynamically switches between backward ($-\hat{z}$) and forward ($+\hat{z}$) scattering. To minimize any in-plane scattering (i.e., endfire), we consider a square-shaped four-element antenna with spacing of $d = \lambda/2 = 5.3$ μm (Figure 2A). As in the previous case, we start at the high-frequency side of the MD resonance (Figure 2B). In this regime, the relative phase between the ED and MD modes rapidly diverges. At a sphere radius of $r = 1.41$ μm, the relative phase shift and thus the backscattering ($-\hat{z}$) intensity are maximized (Figure 2C). Through free-carrier refraction, we can blue-shift the resonances and achieve the Kerker condition (Figure 2D). When all of the spheres are uniformly pumped to a free carrier density of 7×10^{17} cm^{-3}, a unidirectional beam is formed along the $+\hat{z}$ direction (Figure 2C). Therefore, we can reconfigurably steer the antenna lobe along the $+\hat{z}$ or $-\hat{z}$ axis by modulating the free-carrier concentration.

Huygens Metasurface. Extending the design principle of finite arrays of resonators, we form an infinite planar phased array of resonators, which are ideal Huygens sources[56,57] that enable full control of the optical wavefront.[58,59] Just as single resonators exhibit pure forward scattering at the Kerker condition, an infinite array of resonators supporting spectrally overlapping ED and MD modes exhibits unity transmission. As the resonances interfere with the incident plane wave, each mode can impart a phase shift of up to π, leading to a total possible phase shift of 2π. By combining this principle with free-carrier refraction, one can achieve metasurfaces with near-unity transmission and full 2π phase tuning. Below we describe two design principles that rely on different phenomena to achieve the desired overlap of ED and MD resonances.

To understand the difference between single resonators and infinite arrays, we investigate the transmission of a linearly polarized plane wave through an infinite square array of spheres with uniform radius r and periodicity d (Figure 3A). For periodicities close to but smaller than the wavelength ($0.8 < d/\lambda < 1$), the complex transmission coefficient t can be calculated using an analytical coupled-dipole model based on a periodic Green's function (G^{∞})[3,60] with effective magnetic and electric Mie polarizabilities (α_m and α_e, respectively):[61]

$$t = 1 + \frac{ik}{2d^2}\left(\frac{1}{\epsilon_0/\alpha_e - G^{\infty}} + \frac{1}{1/\alpha_m - G^{\infty}}\right) \quad (3)$$

where $k = 2\pi/\lambda$, $\alpha_m = (6\pi i/k^3)b_1$, $\alpha_e = (6\pi i/\epsilon_0 k^3)a_1$, and

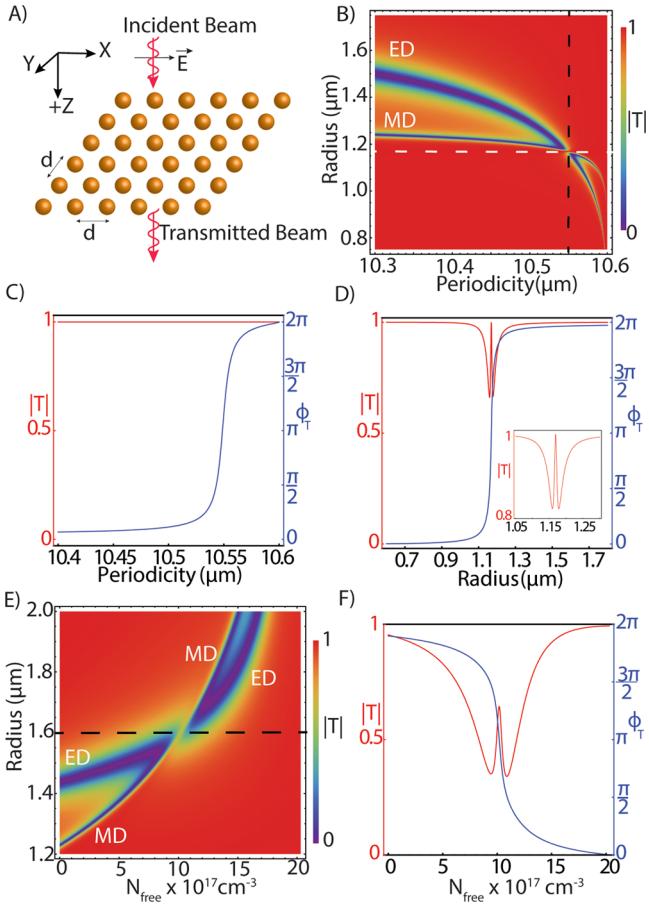

Figure 3. (A) Sketch of the infinite array of spheres of radius r in a square lattice arrangement with periodicity d along the $\hat{x}$ and $\hat{y}$ axes. The array is excited by a linearly polarized plane wave traveling along the $+\hat{z}$ direction. (B) Transmission coefficient at $\lambda = 10.6$ μm as a function of r and d when no charge carriers are present in the system. The plot shows ED and MD modes crossing to form a Huygens source at $r = 1.17$ μm and $d = 10.55$ μm. The white dashed line corresponds to panel C, while the black dashed line corresponds to panel D. (C) Transmission as a function of periodicity at the mode-crossing condition (white dashed line in panel B). The transmission amplitude (red) stays constant while the phase (blue) varies by 2π. (D) Transmission as a function of radius at the mode-crossing condition (black dashed line in panel B). The transmission amplitude (red) goes through an EIT-like line shape (detailed in the inset) while the phase (blue) varies by 2π. (E) Transmission as a function of radius and free carrier concentration for an array periodicity of 10.38 μm, showing that the mode-crossing condition can be achieved by tuning the charge carrier density in the resonators. The black dashed line corresponds to panel F. (F) Transmission as a function of charge carrier density for a Huygens metasurface with $r = 1.6$ μm and $d = 10.38$ μm. The behavior is similar to that shown in panel D: the transmission amplitude demonstrates an EIT-like line shape while the phase varies by 2π.

$$G^{\infty} = \frac{1}{4\pi}\left[\frac{4\pi^2\sqrt{2}}{d^3\sqrt{\frac{\lambda}{d} - 1}} - \frac{118}{d^3} + i\left(\frac{2\pi k}{d^2} - \frac{2k^3}{3}\right)\right] \quad (4)$$

We intentionally consider subwavelength periodicities, so there are no diffraction lobes. The transmitted intensity ($T = |t|^2$) for arrays of different radii and periodicities are plotted in Figure 3B. The ED and MD resonances appear as large dips in transmission. At small periodicities, the array resonance

DOI: 10.1021/acsphotonics.5b00132
ACS Photonics 2015, 2, 1077−1084

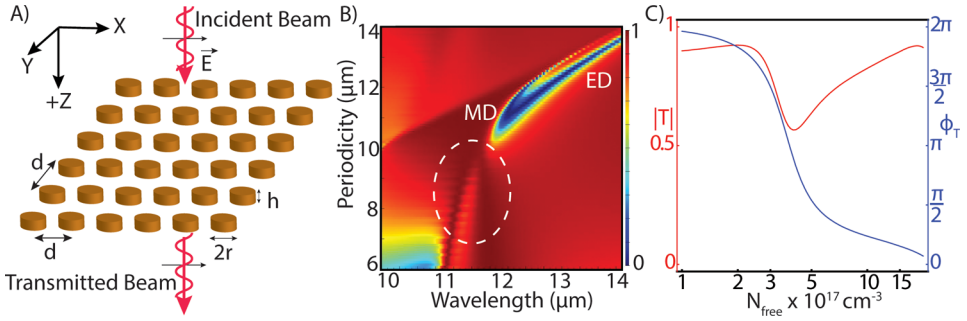

Figure 4. (A) Schematic showing an array of InSb microdisks excited by a linearly polarized plane wave. (B) Plot of the transmission amplitude as a function of periodicity d and wavelength λ for a uniform array of disks with radius r = 2 μm and height h = 1.7 μm. The dashed white ellipse a region where the ED and MD modes spectrally overlap to give near-unity transmission. (C) Plot of the phase and intensity of the transmission coefficient as functions of charge carrier density through a uniform array of microdisks with r = 2 μm and h = 1.7 μm with a square lattice periodicity of 8 μm. The transmission phase varies by 2π while the amplitude varies by less than 2.5 dB.

wavelengths are identical to those for single resonators (MD and ED resonances at $n\rho \approx 0.48$ and 0.64, respectively), as expected for systems with weak interparticle coupling.

However, the resonance line shapes and line widths of the array are strongly modified compared with those of single particles. In particular, the Q factor of the ED and MD resonances increases by approximately 500% (Figure S8 in the Supporting Information). Unlike single particles, which can scatter radiation in any direction, the arrays can reradiate into only two channels: normal-incidence transmission and reflection. Since the individual resonator bandwidths are radiation-limited,[40] this reduction in scattering channels leads to narrow, Lorentzian line shapes. As the array periodicity approaches the wavelength, the ED and MD resonances both shift to smaller particle radii (i.e., smaller normalized frequency) as a result of coupling to lattice resonances.[62,63] Leveraging their different dispersion, we can design the array parameters to achieve overlapping ED and MD resonances at our operating wavelength (λ = 10.6 μm). At r = 1.17 μm and d = 10.55 μm, the ED and MD modes intersect, and the array exhibits unity transmission (Figure 3B). The radius where the ED and MD modes intersect is identical to the Kerker radius for a single sphere (ρ = 0.11). In analogy with single spheres and pure forward scattering at this condition, the effective electric and magnetic polarizabilities are identical, and the transmission amplitude is unity for *all* periodicities. As the periodicity is varied, the effective polarizabilities trace out identical resonances; the transmission phase rapidly undergoes a phase shift of 2π while maintaining an amplitude of unity (Figure 3C). Operating near the ED/MD mode crossing, one could exploit different-sized resonators to achieve 2π phase variation and near-constant transmission. A vertical line cut through the ED/MD mode crossing (black dashed line in Figure 3B) is shown in Figure 3D. The transmission is at a maximum at the mode crossing (r = 1.17 μm) with small dips on either side due to mismatching ED and MD dispersions. The transmission maximum at spectral overlap is analogous to electromagnetically induced transparency (EIT)[64] and occurs because of coupling of two distinct modes within the same resonator.[2,65] About this point, the transmission phase undergoes a full 2π phase shift with less than 20% variation in transmission intensity.

Following this behavior with size engineering, we design a reconfigurable Huygens metasurface by examining the effects of pumping charge carriers into the resonators (see the Supporting Information for a video showing the variation of Figure 3B with increasing carrier concentration). Similar to our broadside and endfire antenna designs, the ED/MD mode crossing shifts to larger normalized size parameter (i.e., larger radius or smaller wavelength) with increasing carrier density. In Figure 3E, we plot the transmission amplitude as a function of particle size and free carrier concentration for an array periodicity d = 10.38 μm. The ED/MD crossover occurs only for a specific particle radius (r = 1.6 μm). For this radius, a line cut (black line in Figure 3E) demonstrating the free-carrier-dependent transmission phase and amplitude is shown in Figure 3F. As in the previously considered antennas, we begin detuned to the high-frequency side of the desired resonances. The incident wave weakly interacts with the array and is transmitted with unity amplitude and no phase shift ($\phi_t = 2\pi$). As free carriers are introduced into the resonators, the ED and MD modes both shift to higher frequency, passing through crossover at $N_{free} = 1 \times 10^{18}$ cm^{-3}. As the ED and MD modes pass through the Kerker condition, the transmission phase drops to zero. At crossover, the transmission amplitude goes through a local maximum but does not reach unity because of free-carrier-induced losses. The free-carrier-dependent behavior mimics that of varying particle size (Figure 3D), albeit with increased losses. Thus, we describe a reconfigurable infrared metasurface on which the transmission phase can be varied between 0 and 2π with less than 4 dB loss in intensity.

As can be seen from eq 3, arrays of resonators that *individually* exhibit overlapping ED and MD modes also exhibit overlapping resonances in arrays of *any periodicity*. In the spherical silicon resonators described above, there is no radius at which the ED and MD modes overlap. To get overlapping ED and MD modes in a single resonator, we need an extra degree of freedom. One approach, which is also amenable to conventional fabrication techniques, is to use truncated cylindrical structures[66] (or dielectric resonator antennas (DRAs)[67]) that exhibit multipolar resonances analogous to those of spherical particles. By changing the height h and radius r of these resonators, one can independently control the resonance frequencies of the MD and ED modes (see section S9 in the Supporting Information for the geometric dispersion analysis). For a suitably chosen aspect ratio (r/h = 1.17), subwavelength DRA arrays exhibit identical ED and MD resonance frequencies and line shapes regardless of periodicity (Figure 4B). In previous studies, this phenomenon has been used to construct phased-array metamaterials from resonators of fixed aspect ratio but varying size.[41] The wavelength- and periodicity-dependent transmission through an array of DRAs

DOI: 10.1021/acsphotonics.5b00132
ACS Photonics 2015, 2, 1077−1084

with an aspect ratio of 1.17 is shown in Figure 4B. For reconfigurable arrays, we start detuned to high frequency; the resonator size (r = 2 μm, h = 1.7 μm) is chosen so that the ED/MD resonance wavelength occurs at 11 μm. At the operating wavelength (10.6 μm), the transmission depends on the periodicity but remains near unity ($T > 0.9$) for periodicities between 8 and 10 μm. We find optimal tunability for arrays with d = 8 μm: the free-carrier-dependent transmission amplitude and phase for such an array are shown in Figure 4C. The array shows 2π phase variation with losses less than 2.5 dB. We also find that introduction of a substrate does not alter the phase modulation properties of the microdisk array but does increase the transmission loss to about 3−4 dB (see section S10 in the Supporting Information) Again, the use of tunable semiconductor elements enables a reconfigurable metasurface exhibiting 2π phase shifts in transmission with minimal reflection or absorption losses.

In conclusion, we have demonstrated how free-carrier refraction could be leveraged to control the phase and amplitude of scattered fields from individual infrared semiconductor Mie resonators. Using either interference between multiple antennas or interference between different multipolar resonances, we have described reconfigurable endfire and broadside few-element antennas. Building from these results, we have used analytical Green's function calculations and numerical simulations to study phase-variable metasurfaces. We have shown that near-unity transmission with variable phase can be achieved either by coupling individual resonator modes to array lattice resonances or by properly engineering the dimensions of DRA structures. We have shown that free-carrier refraction can be used to drive such arrays through the Kerker condition, enabling phase shifts of 2π with near-unity transmission. The enhancement in the quality factors of the resonances in an infinite array metasurface reduces the required index modulation of the resonators to obtain the 2π phase shift. Experimental realization of such metasurfaces would demand a method to pump each of the resonators individually over a large area. This can be achieved optically with a visible-frequency pump beam coupled to a spatial light modulator.[49] In this way, few-micron-scale variations in visible-frequency light intensity could be translated into subwavelength variations in infrared phase. Ultimately, these design criteria can be applied across the metasurface to form arbitrary spatial phase gradients that lead to reconfigurable flat lenses, dynamic beam-steering antenna systems, etc. Such tunable Huygens metasurfaces made of low-loss III−V semiconductors may form the basis for reconfigurable phased-array metadevices that enable unprecedented control over mid-infrared radiation.

METHODS

Simulations of Antenna Radiation Patterns. Few-element antenna radiation patterns were calculated using the Wave Optics module in the COMSOL Multiphysics finite-element method solver. A tetrahedral mesh with a maximum element size of one-sixth of the local wavelength was used to ensure that mode patterns were accurately computed. For simulations of semiconductor spheres in free space, a spherical perfectly matched layer (PML) was used to minimize reflections at the boundaries. Simulations of semiconductor spheres above a reflective surface were defined by a rectangular cuboid with a gold slab and perfect electric conductor (PEC) boundary condition on the bottom surface and PML boundary conditions on all of the other surfaces. For simulations with reflection symmetries, the appropriate PEC and PML boundary conditions were used to improve the computational efficiency. The scattered field was obtained with a background plane-wave source. The far-field scattering properties were computed using the far-field calculation module, which extrapolates the far-field scattering properties from the near fields using the Stratton−Chu formula.

Simulations of Antenna Array Scattering Parameters. The antenna array scattering parameters were calculated using a commercial-grade simulator (from Lumerical Inc.) based on the finite-difference time-domain method. A nonuniform conformal mesh with a maximum mesh element size of 100 nm along the in-plane direction and a maximum mesh element size of 10 nm along the out-of-plane directions was used. Simulations were run long enough to ensure that fields from high-quality-factor resonances decayed less than 1 part in a millionth of the incident field. PML boundary conditions were used on the top and bottom surfaces. A symmetric periodic boundary condition was used along the polarization direction and an antisymmetric periodic boundary condition normal to the polarization direction to improve the computational efficiency. The reflection and transmission coefficients were computed using the "S parameter" analysis object,[68,69] which makes use of a plane-wave excitation source.

ASSOCIATED CONTENT

Supporting Information

A brief description of the methods used for numerical evaluation and additional data supporting the results in the main text. The Supporting Information is available free of charge on the ACS Publications website at DOI: 10.1021/acsphotonics.5b00132.

AUTHOR INFORMATION

Corresponding Author

*E-mail: jonschuller@ece.ucsb.edu.

Author Contributions

P.P.I. and J.A.S. proposed and conceived the idea and developed the analytical Mie theory framework. P.P.I. and N.A.B. performed the numerical simulations. N.A.B. helped P.P.I. in the Green's function analysis. P.P.I. and J.A.S. analyzed the data and wrote the manuscript.

Notes

The authors declare no competing financial interest.

ACKNOWLEDGMENTS

This work was supported by the Air Force Office of Scientific Research Young Investigator Program (FA9550-13-1-0182). We also acknowledge support from the Centre for Scientific Computing of the California NanoSystems Institute (CNSI) Materials Research Laboratory (MRL), an NSF MRSEC (DMR-1121053), and NSF CNS-0960316. N.A.B. acknowledges support through a Department of Defense NDSEG Fellowship.

REFERENCES

(1) Dregely, D.; Taubert, R.; Dorfmüller, J.; Vogelgesang, R.; Kern, K.; Giessen, H. 3D Optical Yagi−Uda Nanoantenna Array. *Nat. Commun.* **2011**, *2*, No. 267.

(2) Yang, Y.; Kravchenko, I. I.; Briggs, D. P.; Valentine, J. All-Dielectric Metasurface Analogue of Electromagnetically Induced Transparency. *Nat. Commun.* **2014**, *5*, No. 5753.

DOI: 10.1021/acsphotonics.5b00132
ACS Photonics 2015, 2, 1077−1084

(3) Špačková, B.; Homola, J. Sensing Properties of Lattice Resonances of 2D Metal Nanoparticle Arrays: An Analytical Model. *Opt. Express* **2013**, *21*, 27490−27502.
(4) Beausoleil, R. G.; Kuekes, P. J.; Snider, G. S.; Wang, S.-Y.; Williams, R. S. Nanoelectronic and Nanophotonic Interconnect. *Proc. IEEE* **2008**, *96*, 230−247.
(5) Yu, N.; Capasso, F. Flat Optics with Designer Metasurfaces. *Nat. Mater.* **2014**, *13*, 139−150.
(6) Kildishev, A. V.; Boltasseva, A.; Shalaev, V. M. Planar Photonics with Metasurfaces. *Science* **2013**, *339*, No. 1232009.
(7) Lévesque, Q.; Makhsiyan, M.; Bouchon, P.; Pardo, F.; Jaeck, J.; Bardou, N.; Dupuis, C.; Haïdar, R.; Pelouard, J.-L. Plasmonic Planar Antenna for Wideband and Efficient Linear Polarization Conversion. *Appl. Phys. Lett.* **2014**, *104*, No. 111105.
(8) Ma, H. F.; Wang, G. Z.; Kong, G. S.; Cui, T. J. Broadband Circular and Linear Polarization Conversions Realized by Thin Birefringent Reflective Metasurfaces. *Opt. Mater. Express* **2014**, *4*, 1717−1724.
(9) Veysi, M.; Guclu, C.; Boyraz, O.; Capolino, F. Thin Anisotropic Metasurfaces for Simultaneous Light Focusing and Polarization Manipulation. *J. Opt. Soc. Am. B* **2015**, *32*, 318−323.
(10) Larouche, S.; Tsai, Y.-J.; Tyler, T.; Jokerst, N. M.; Smith, D. R. Infrared Metamaterial Phase Holograms. *Nat. Mater.* **2012**, *11*, 450−454.
(11) Yang, Y.; Wang, W.; Moitra, P.; Kravchenko, I. I.; Briggs, D. P.; Valentine, J. Dielectric Meta-Reflectarray for Broadband Linear Polarization Conversion and Optical Vortex Generation. *Nano Lett.* **2014**, *14*, 1394−1399.
(12) Aieta, F.; Kats, M. A.; Genevet, P.; Capasso, F. Multiwavelength Achromatic Metasurfaces by Dispersive Phase Compensation. *Science* **2015**, *347*, 1342−1345.
(13) Aieta, F.; Genevet, P.; Kats, M. A.; Yu, N.; Blanchard, R.; Gaburro, Z.; Capasso, F. Aberration-Free Ultrathin Flat Lenses and Axicons at Telecom Wavelengths Based on Plasmonic Metasurfaces. *Nano Lett.* **2012**, *12*, 4932−4936.
(14) Goodman, J. W. *Introduction to Fourier Optics*, 2nd ed.; McGraw-Hill Series in Electrical and Computer Engineering; McGraw-Hill: New York, 1996.
(15) Schuck, P. J.; Fromm, D. P.; Sundaramurthy, A.; Kino, G. S.; Moerner, W. E. Improving the Mismatch between Light and Nanoscale Objects with Gold Bowtie Nanoantennas. *Phys. Rev. Lett.* **2005**, *94*, No. 017402.
(16) Mühlschlegel, P.; Eisler, H.-J.; Martin, O. J. F.; Hecht, B.; Pohl, D. W. Resonant Optical Antennas. *Science* **2005**, *308*, 1607−1609.
(17) Hancu, I. M.; Curto, A. G.; Castro-López, M.; Kuttge, M.; van Hulst, N. F. Multipolar Interference for Directed Light Emission. *Nano Lett.* **2014**, *14*, 166−171.
(18) Schuller, J. A.; Barnard, E. S.; Cai, W.; Jun, Y. C.; White, J. S.; Brongersma, M. L. Plasmonics for Extreme Light Concentration and Manipulation. *Nat. Mater.* **2010**, *9*, 193−204.
(19) Taminiau, T. H.; Stefani, F. D.; van Hulst, N. F. Enhanced Directional Excitation and Emission of Single Emitters by a Nano-Optical Yagi−Uda Antenna. *Opt. Express* **2008**, *16*, 10858−10866.
(20) Stout, B.; Devilez, A.; Rolly, B.; Bonod, N. Multipole Methods for Nanoantennas Design: Applications to Yagi−Uda Configurations. *J. Opt. Soc. Am. B* **2011**, *28*, 1213−1223.
(21) Sun, S.; He, Q.; Xiao, S.; Xu, Q.; Li, X.; Zhou, L. Gradient-Index Meta-Surfaces as a Bridge Linking Propagating Waves and Surface Waves. *Nat. Mater.* **2012**, *11*, 426−431.
(22) Ahmadi, A.; Ghadarghadr, S.; Mosallaei, H. An Optical Reflectarray Nanoantenna: The Concept and Design. *Opt. Express* **2010**, *18*, 123−133.
(23) Li, Z.; Huang, L.; Lu, K.; Sun, Y.; Min, L. Continuous Metasurface for High-Performance Anomalous Reflection. *Appl. Phys. Express* **2014**, *7*, No. 112001.
(24) Li, Z.; Palacios, E.; Butun, S.; Aydin, K. Visible-Frequency Metasurfaces for Broadband Anomalous Reflection and High-Efficiency Specrum Splitting. *Nano Lett.* **2015**, *15*, 1615−1621.
(25) Sieber, P. E.; Werner, D. H. Infrared Broadband Quarter-Wave and Half-Wave Plates Synthesized from Anisotropic Bézier Metasurfaces. *Opt. Express* **2014**, *22*, 32371−32383.
(26) Liu, A. Q.; Zhu, W. M.; Tsai, D. P.; Zheludev, N. I. Micromachined Tunable Metamaterials: A Review. *J. Opt.* **2012**, *14*, No. 114009.
(27) Michel, A.-K. U.; Chigrin, D. N.; Maß, T. W. W.; Schönauer, K.; Salinga, M.; Wuttig, M.; Taubner, T. Using Low-Loss Phase-Change Materials for Mid-Infrared Antenna Resonance Tuning. *Nano Lett.* **2013**, *13*, 3470−3475.
(28) Emani, N. K.; Chung, T.-F.; Kildishev, A. V.; Shalaev, V. M.; Chen, Y. P.; Boltasseva, A. Electrical Modulation of Fano Resonance in Plasmonic Nanostructures Using Graphene. *Nano Lett.* **2014**, *14*, 78−82.
(29) Lu, F.; Liu, B.; Shen, S. Infrared Wavefront Control Based on Graphene Metasurfaces. *Adv. Opt. Mater.* **2014**, *2*, 794−799.
(30) Jun, Y. C.; Brener, I. Electrically Tunable Infrared Metamaterials Based on Depletion-Type Semiconductor Devices. *J. Opt.* **2012**, *14*, No. 114013.
(31) Zheludev, N. I.; Kivshar, Y. S. From Metamaterials to Metadevices. *Nat. Mater.* **2012**, *11*, 917−924.
(32) Brongersma, M. L.; Cui, Y.; Fan, S. Light Management for Photovoltaics Using High-Index Nanostructures. *Nat. Mater.* **2014**, *13*, 451−460.
(33) Mann, S. A.; Grote, R. R.; Osgood, R. M.; Schuller, J. A. Dielectric Particle and Void Resonators for Thin Film Solar Cell Textures. *Opt. Express* **2011**, *19*, 25729−25740.
(34) Cao, L.; Park, J.-S.; Fan, P.; Clemens, B.; Brongersma, M. L. Resonant Germanium Nanoantenna Photodetectors. *Nano Lett.* **2010**, *10*, 1229−1233.
(35) Schuller, J. A.; Taubner, T.; Brongersma, M. L. Optical Antenna Thermal Emitters. *Nat. Photonics* **2009**, *3*, 658−661.
(36) Miyazaki, H. T.; Kasaya, T.; Iwanaga, M.; Choi, B.; Sugimoto, Y.; Sakoda, K. Dual-Band Infrared Metasurface Thermal Emitter for CO_2 Sensing. *Appl. Phys. Lett.* **2014**, *105*, No. 121107.
(37) Fu, Y. H.; Kuznetsov, A. I.; Miroshnichenko, A. E.; Yu, Y. F.; Luk'yanchuk, B. Directional Visible Light Scattering by Silicon Nanoparticles. *Nat. Commun.* **2013**, *4*, No. 1527.
(38) Krasnok, A. E.; Miroshnichenko, A. E.; Belov, P. A.; Kivshar, Y. S. All-Dielectric Optical Nanoantennas. *AIP Conf. Proc.* **2012**, *1475*, 22−24.
(39) Munárriz, J.; Malyshev, A. V.; Malyshev, V. A.; Knoester, J. Optical Nanoantennas with Tunable Radiation Patterns. *Nano Lett.* **2013**, *13*, 444−450.
(40) Schuller, J. A.; Brongersma, M. L. General Properties of Dielectric Optical Antennas. *Opt. Express* **2009**, *17*, 24084−24095.
(41) Decker, M.; Staude, I.; Falkner, M.; Dominguez, J.; Neshev, D. N.; Brener, I.; Pertsch, T.; Kivshar, Y. S. High-Efficiency Dielectric Huygens' Surfaces. *Adv. Opt. Mater.* **2015**, *3*, 813−820.
(42) Zou, L.; Withayachumnankul, W.; Shah, C. M.; Mitchell, A.; Bhaskaran, M.; Sriram, S.; Fumeaux, C. Dielectric Resonator Nanoantennas at Visible Frequencies. *Opt. Express* **2013**, *21*, 1344−1352.
(43) Lin, D.; Fan, P.; Hasman, E.; Brongersma, M. L. Dielectric Gradient Metasurface Optical Elements. *Science* **2014**, *345*, 298−302.
(44) Bohren, C. F.; Huffman, D. R. *Absorption and Scattering of Light by Small Particles*; Wiley-VCH: Weinheim, Germany, 2008.
(45) Wei, L.; Miroshnichenko, A. E.; Kivshar, Y. S. Control of Light Scattering by Nanoparticles with Optically-Induced Magnetic Responses. *Chin. Phys. B* **2014**, *23*, 047806.
(46) Bennett, B. R.; Soref, R. A.; del Alamo, J. A. Carrier-Induced Change in Refractive Index of InP, GaAs and InGaAsP. *IEEE J. Quantum Electron.* **1990**, *26*, 113−122.
(47) Nedeljkovic, M.; Soref, R.; Mashanovich, G. Z. Free-Carrier Electrorefraction and Electroabsorption Modulation Predictions for Silicon over the 1−14 μm Infrared Wavelength Range. *IEEE Photonics J.* **2011**, *3*, 1171−1180.
(48) Chen, H.-T.; O'Hara, J. F.; Azad, A. K.; Taylor, A. J.; Averitt, R. D.; Shrekenhamer, D. B.; Padilla, W. J. Experimental Demonstration of

DOI: 10.1021/acsphotonics.5b00132
ACS Photonics 2015, 2, 1077−1084

Frequency-Agile Terahertz Metamaterials. *Nat. Photonics* **2008**, *2*, 295−298.
(49) Hayasaki, Y.; Sugimoto, T.; Takita, A.; Nishida, N. Variable Holographic Femtosecond Laser Processing by Use of a Spatial Light Modulator. *Appl. Phys. Lett.* **2005**, *87*, No. 031101.
(50) Yu, P. Y.; Cardona, M. *Fundamentals of Semiconductors*, 4th ed.; Graduate Texts in Physics; Springer: Berlin, 2010.
(51) Law, S.; Adams, D. C.; Taylor, A. M.; Wasserman, D. Mid-Infrared Designer Metals. *Opt. Express* **2012**, *20*, 12155−12165.
(52) Wagner, M.; McLeod, A. S.; Maddox, S. J.; Fei, Z.; Liu, M.; Averitt, R. D.; Fogler, M. M.; Bank, S. R.; Keilmann, F.; Basov, D. N. Ultrafast Dynamics of Surface Plasmons in InAs by Time-Resolved Infrared Nanospectroscopy. *Nano Lett.* **2014**, *14*, 4529−4534.
(53) Law, S.; Liu, R.; Wasserman, D. Doped Semiconductors with Band-Edge Plasma Frequencies. *J. Vac. Sci. Technol., B* **2014**, *32*, No. 052601.
(54) Janke, C.; Rivas, J. G.; Bolivar, P. H.; Kurz, H. All-Optical Switching of the Transmission of Electromagnetic Radiation through Subwavelength Apertures. *Opt. Lett.* **2005**, *30*, 2357−2359.
(55) Kerker, M.; Wang, D.-S.; Giles, C. L. Electromagnetic Scattering by Magnetic Spheres. *J. Opt. Sci. Am.* **1983**, *73*, 765−767.
(56) Huygens, C. *Treatise on Light*; tredition: Hamburg, Germany, 2012
(57) Love, A. E. H. The Integration of the Equations of Propagation of Electric Waves. *Philos. Trans. R. Soc., A* **1901**, *197*, 1−45.
(58) Holloway, C. L.; Mohamed, M. A.; Kuester, E. F.; Dienstfrey, A. Reflection and Transmission Properties of a Metafilm: With an Application to a Controllable Surface Composed of Resonant Particles. *IEEE Trans. Electromagn. Compat.* **2005**, *47*, 853−865.
(59) Pfeiffer, C.; Grbic, A. Metamaterial Huygens' Surfaces: Tailoring Wave Fronts with Reflectionless Sheets. *Phys. Rev. Lett.* **2013**, *110*, No. 197401.
(60) García de Abajo, F. J. Colloquium: Light Scattering by Particle and Hole Arrays. *Rev. Mod. Phys.* **2007**, *79*, 1267−1290.
(61) Evlyukhin, A. B.; Reinhardt, C.; Seidel, A.; Luk'yanchuk, B. S.; Chichkov, B. N. Optical Response Features of Si-Nanoparticle Arrays. *Phys. Rev. B* **2010**, *82*, No. 045404.
(62) Karagodsky, V.; Sedgwick, F. G.; Chang-Hasnain, C. J. Theoretical Analysis of Subwavelength High Contrast Grating Reflectors. *Opt. Express* **2010**, *18*, 16973−16988.
(63) Väkeväinen, A. I.; Moerland, R. J.; Rekola, H. T.; Eskelinen, A.-P.; Martikainen, J.-P.; Kim, D.-H.; Törmä, P. Plasmonic Surface Lattice Resonances at the Strong Coupling Regime. *Nano Lett.* **2014**, *14*, 1721−1727.
(64) Marangos, J. P. Electromagnetically Induced Transparency. *J. Mod. Opt.* **1998**, *45*, 471−503.
(65) Gu, J.; Singh, R.; Liu, X.; Zhang, X.; Ma, Y.; Zhang, S.; Maier, S. A.; Tian, Z.; Azad, A. K.; Chen, H.-T.; Taylor, A. J.; Han, J.; Zhang, W. Active Control of Electromagnetically Induced Transparency Analogue in Terahertz Metamaterials. *Nat. Commun.* **2012**, *3*, No. 1151.
(66) Staude, I.; Miroshnichenko, A. E.; Decker, M.; Fofang, N. T.; Liu, S.; Gonzales, E.; Dominguez, J.; Luk, T. S.; Neshev, D. N.; Brener, I.; Kivshar, Y. Tailoring Directional Scattering through Magnetic and Electric Resonances in Subwavelength Silicon Nanodisks. *ACS Nano* **2013**, *7*, 7824−7832.
(67) Mongia, R. K.; Bhartia, P. Dielectric Resonator Antennas—A Review and General Design Relations for Resonant Frequency and Bandwidth. *Int. J. Microwave Millimeter-Wave Comput.-Aided Eng.* **1994**, *4*, 230−247.
(68) Smith, D. R.; Vier, D. C.; Koschny, T.; Soukoulis, C. M. Electromagnetic Parameter Retrieval from Inhomogeneous Metamaterials. *Phys. Rev. E* **2005**, *71*, 1−11.
(69) Szabó, Z.; Park, G. H.; Hedge, R.; Li, E. P. A Unique Extraction of Metamaterial Parameters Based on Kramers−Kronig Relationship. *IEEE Trans. Microwave Theory Technol.* **2010**, *58*, 2646−2653.

DOI: 10.1021/acsphotonics.5b00132
ACS Photonics 2015, 2, 1077−1084